AGU PUBLICATIONS

JGR

Journal of Geophysical Research: Space Physics

RESEARCH ARTICLE
10.1002/2014JA020184

Key Points:
- Propagation of spread F and gravity waves in the low-latitude ionosphere
- One year observation by multipoint continuous Doppler sounding system
- Determination of azimuths and horizontal velocities of propagation

Correspondence to:
J. Chum,
jachu@ufa.cas.cz

Citation:
Chum, J., et al. (2014), Propagation of gravity waves and spread *F* in the low-latitude ionosphere over Tucumán, Argentina, by continuous Doppler sounding: First results, *J. Geophys. Res. Space Physics*, *119*, 6954–6965, doi:10.1002/2014JA020184.

Received 19 MAY 2014
Accepted 6 AUG 2014
Accepted article online 11 AUG 2014
Published online 28 AUG 2014

Propagation of gravity waves and spread *F* in the low-latitude ionosphere over Tucumán, Argentina, by continuous Doppler sounding: First results

J. Chum[1], F. A. M. Bonomi[2], J. Fišer[1], M. A. Cabrera[2,3], R. G. Ezquer[3,4,5], D. Burešová[6], J. Laštovička[6], J. Baše[1], F. Hruška[1], M. G. Molina[7], J. E. Ise[2], J. I. Cangemi[2], and T. Šindelářová[6]

[1]Department of Upper Atmosphere, Institute of Atmospheric Physics, Prague, Czech Republic, [2]Laboratorio de Telecomunicaciones, FACET, Universidad Nacional de Tucumán, Tucumán, Argentina, [3]Centro de Investigación de Atmósfera Superior y Radiopropagación, Facultad Regional Tucumán, Universidad Tecnológica Nacional, Buenos Aires, Argentina, [4]Laboratorio de Ionósfera, FACET, Universidad Nacional de Tucumán, Tucumán, Argentina, [5]CONICET, Buenos Aires, Argentina, [6]Department of Aeronomy, Institute of Atmospheric Physics, Prague, Czech Republic, [7]Departamento de Ciencias de la Computacio, FACET, Universidad Nacional de Tucumán, Tucumán, Argentina

Abstract Results of systematic analysis of propagation directions and horizontal velocities of gravity waves (GWs) and spread *F* structures in low-latitude ionosphere (magnetic inclination ~27°) in Tucumán region, Argentina, are presented. Measurements were carried out by multipoint continuous Doppler system during 1 year from December 2012 to November 2013. It was found that meridian propagation of GWs dominated and that southward propagation prevailed in the local summer. Oblique spread structures observed in Doppler shift spectrograms and associated with spread *F* propagated roughly eastward at velocities from ~70 to ~180 m/s and were observed at night from ~ September to ~ March. The velocities were computed for 182 events and the azimuths for 64 events. Continuous Doppler sounding makes it possible to analyze more events compared to optical observations often used for propagation studies since the measurements do not depend on weather.

1. Introduction

Atmospheric gravity waves (GWs) and ionospheric irregularities like spread *F* can change conditions for propagation of radio signals in the ionosphere, including the Global Positioning System (GPS) [*Nishioka et al*., 2013; *Ezquer et al*., 2003; *McNamara et al*., 2008]. GWs represent an important coupling mechanism between the lower and upper atmosphere [*Hocke and Schlegel*, 1996; *Fritts and Alexander*, 2003; *Laštovička*, 2006; *Vadas*, 2007]. They have been investigated in a large number of studies since the pioneering work by *Hines* [1960]. On the other hand, the equatorial spread *F* and plasma bubbles are irregularities that are believed to result from Rayleigh-Tailor instability triggered mainly by the uplift of the *F* layer owing to the prereversal enhancement of the eastward (zonal) electric field [*Fejer et al*., 1999; *Kelley*, 2009; *Abdu et al*., 2009a, and references therein]. The day-to-day variability and role of other factors like electron density gradients, conductivity, GWs, and zonal and meridian winds acting as seeding mechanism for the instability are, however, not well understood and are a subject of intense investigation [*Kudeki et al*., 2007; *Abdu et al*., 2009a; *Abdu et al*., 2009b; *Cabrera et al*., 2010].

The propagation of the GWs and ionospheric irregularities in the upper atmosphere and ionosphere can be studied optically or by means of radio signals. In the first case, perturbations of airglow intensity are measured by sensitive all-sky cameras at various wavelengths, usually in visible or near-infrared range, from heights of ~85–100 km [*Isler et al*., 1997; *Dou et al*., 2010] or from altitudes of ~200–300 km [*Shiokawa et al*., 2009; *Haase et al*., 2011]. As for the radio signals, usually, total electron content perturbation measurements by a dense network of dual-frequency GPS receivers [*Nishioka et al*., 2013; *Otsuka et al*., 2013] or observations by continuous Doppler radars [*Crowley and Rodrigues*, 2012; *Chum et al*., 2012a] are used to estimate the horizontal propagation directions and velocities of GWs. The development of ionospheric irregularities can also be studied by pulse radars [*Fejer et al*., 1999]. In this paper, we will present the analysis based on the measurements carried out by multipoint continuous Doppler sounding system (CDSS).

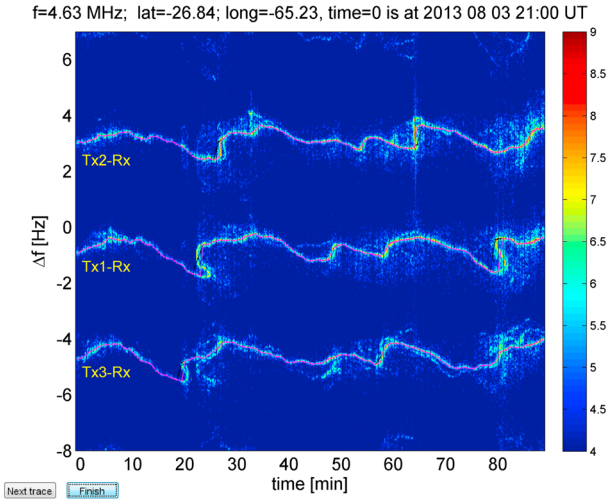

Figure 1. An example of GW observation. A record from 21:00 UT to 22:30 UT on 3 August is presented. From top to bottom are the signals from Tx2, Tx1, and Tx3 transmitters. Magenta lines show the maxima of spectral intensities for individual traces (signals) as single-value functions of time. Black lines (mostly covered by magenta lines) are the output of automatic procedure. See the text for more details.

The continuous Doppler sounding of the ionosphere started around 1960 [*Davies et al.*, 1962; *Davies and Baker*, 1966; *Georges*, 1967] and uses the fact that the sounding radio wave reflects at the region where its frequency matches the local plasma frequency. If a GW causes, via collisions between neutral and charged particles, movement of the reflecting level, then Doppler shift of the sounding radio wave is observed. The Doppler shift can also be excited by magnetohydrodynamic waves causing pulsation of geomagnetic field [*Sutcliffe and Poole*, 1989], by solar X-ray flares [*Liu et al.*, 1996], or by infrasound waves [*Chum et al.*, 2012b; *Šindelářová et al.*, 2009]. In the latter cases, the Doppler shift cannot be simply related to the movement of reflecting layer; e.g., if the air (plasma) fluctuations are caused by infrasound waves, then the compression or rarefaction of the gas can contribute to the observed Doppler shift more than the advection (up and down motion of the reflecting layer) [*Chum et al.*, 2012b].

To study horizontal propagation of ionospheric disturbances by Doppler sounding, at least three spatially separated sounding signals are needed. The time differences between the observations of corresponding signatures (waves) on the different sounding paths are then used to evaluate the observed horizontal velocities. An assumption of plane wave propagation is usually applied for these calculations. Doppler shift spectrograms [*Chum et al.*, 2010] or Doppler shifts as single-valued functions of time [*Crowley and Rodrigues*, 2012] are used in these studies. This article builds on previous research of GW propagation at middle latitudes by multipoint CDSS located in central Europe and South Africa [*Chum et al.*, 2010; 2012a]. There are, however, several differences and extensions in the current report. First, the measurements are carried out in the low-latitude ionosphere, over Tucumán region, Argentina. The results obtained during the first year of operation of this system from December 2012 to November 2013 are presented. Second, the previous studies were predominantly based on short-scale GWs that formed S-shaped signatures in Doppler shift spectrograms. To be able to study also the propagation of GWs with larger horizontal scales that do not form the S-shaped signatures, this restriction is relaxed in this study, and a new method based on slowness search is introduced, though the analysis based on S-shaped signatures is also repeated for consistency. Third, propagation of ionospheric irregularities that form oblique spread structures in Doppler shift spectrograms and can be related to spread *F* or plasma bubbles is investigated. The propagation of equatorial spread *F* and plasma bubbles was studied from optical airglow measurements and GPS data [*Makela and Kelley*, 2003; *Martinis et al.*, 2003; *Terra et al.*, 2004; *Haase et al.*, 2011] or data obtained by modern digisondes [*Reinisch et al.*, 2004] but has not been studied from continuous Doppler sounding to the best of our knowledge.

2. Measurements

The multipoint CDSS consisting of three transmitters Tx1, Tx2, and Tx3 (transmitted power ~1 W) and one receiver Rx was installed in the Tucumán region, Argentina, at the end of November 2012. The CDSS is very similar to the system that was used in previous studies in the Czech Republic and South Africa [*Chum et al.*, 2010; 2012a] except that the sounding frequency of 4.63 MHz was now selected for Tucumán. As in the previous studies, signals from all transmitters are displayed in one Doppler shift spectrogram. An example of GW observation is presented in Figure 1 which shows the measurement from 21:00 UT to 22:30 UT on 3 August 2013. Geographical coordinates and distribution of the individual transmitters and receiver are given in Figure 2; positions of reflection points are assumed in the midway between the transmitters and receiver.

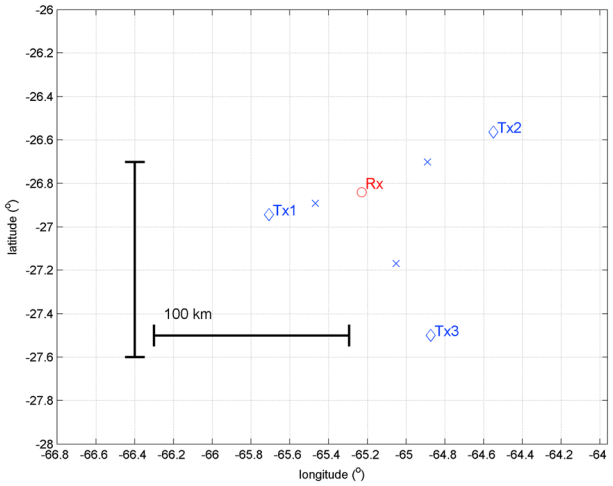

Figure 2. Locations of transmitters Tx1, Tx2, and Tx3 (blue diamonds) and receiver Rx (red circle) in geographical coordinates. Reflection points marked by blue crosses are assumed in the midway between the individual transmitters and the receiver.

The inclination of magnetic field in the region of measurement calculated by the International Geomagnetic Reference Field model is ~27°. The original Doppler shift spectrogram presented in Figure 1 does not provide Doppler shifts as single-valued functions of time which are convenient for mathematical analysis. Therefore, maxima of spectral intensities are found for each sounding path in the Doppler shift spectrogram. These maxima are drawn by magenta line (dots) in Figure 1. The maxima are searched over 1 min spectrum and interpolated into 30 s time resolution for the purpose of GW study. This is first done automatically. The found maxima are then searched visually and if necessary manually corrected. Examples of such corrections can be seen in Figure 1 for all three traces just after ~21:20 UT or for Tx1-Rx trace around 22:20 UT when the S-shaped signatures were observed. The S-shaped signatures were approximated by single-value functions of time manually. The black lines that are mostly covered by magenta lines show the original automatic finding (fit) before the visual inspection and manual approval or correction. Analysis of GW propagation based on the obtained signals will be presented in section 3.

Figure 3 shows an example of the record when the observed Doppler shifts cannot be approximated by single-valued functions of time. (The order of signal paths is different from Figure 1 because of service maintenance of Tx1 and usage of spare piece instead of original Tx1.) Distinct oblique spread structures are observed in the Doppler shift spectrogram during the displayed time interval from 01:00 UT to 07:00 UT on 25 October 2013. A careful inspection of the presented spectrogram reveals that the oblique spread structures are observed with time delays between individual sounding paths. If the starts (ends) of oblique spread structures are sufficiently clear and sharp in the Doppler shift spectrogram, as in Figure 3, it is possible to determine (estimate) the time delays between the structures observed in three different transmitter-receiver paths, and hence, propagation velocities and directions can be estimated. The estimating of the time delays is done manually by clicking in the Doppler shift spectrogram in MATLAB software and should not be mixed up with the slowness method used for GWs presented in section 3. It is necessary to note that not always can the beginning and end of these structures be identified with sufficient accuracy. Statistical analysis of occurrence of these oblique structures and analysis of propagation velocities for distinct cases will be presented in section 4. It will be furthermore shown there that the propagation velocities (not directions) can also be derived from the tilt of the oblique structures in the Doppler shift spectrogram.

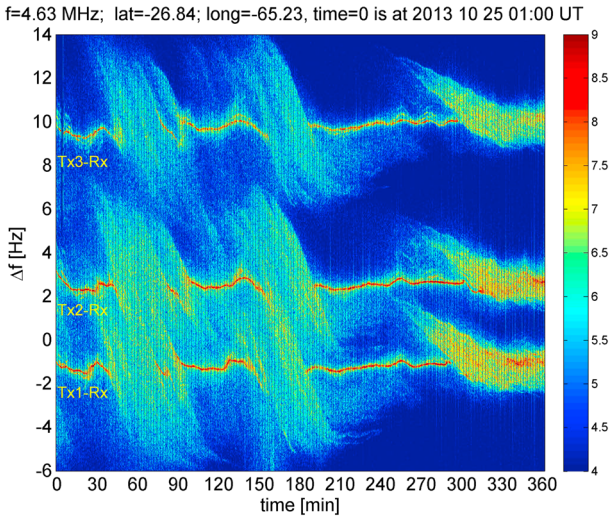

Figure 3. An example of observations of oblique spread structures in Doppler shift spectrogram recorded from 01:00 UT to 07:00 UT on 25 October 2013. From top to bottom are the signals from Tx3, Tx2, and Tx1 transmitters.

The ionosonde located several kilometers from the receiver Rx in San Miguel de

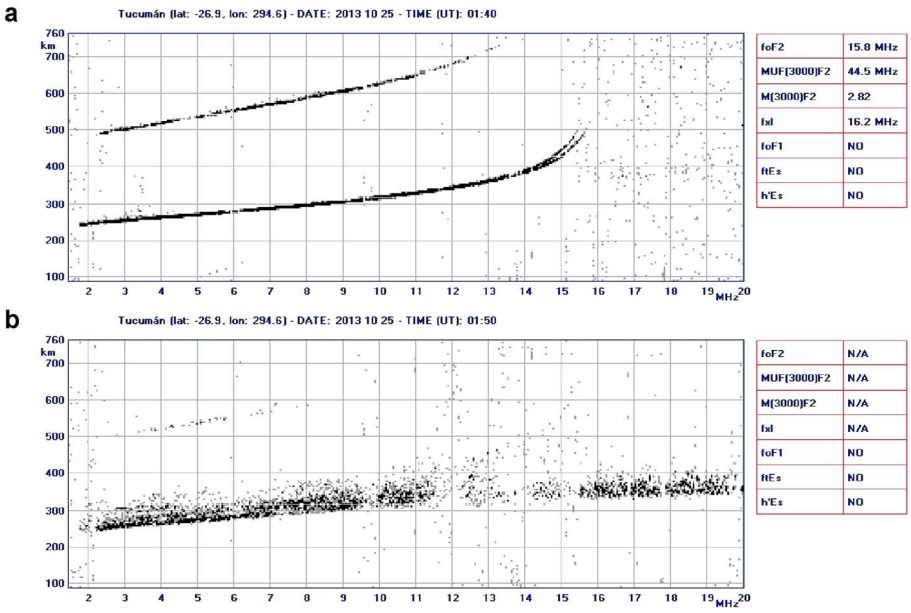

Figure 4. Ionograms recorded in Tucumán at (a) 01:40 UT and (b) 01:50 UT on 25 October 2013.

Tucumán [*Cabrera et al*., 2010] was out of regular operation owing to its upgrade during the study period from December 2012 to November 2013. There were, however, several test runs in October 2013 that enabled simultaneous measurements by ionosonde and CDSS. A comparison of these measurements shows that the oblique spread structures in the Doppler shift spectrogram start at the same time (within the time resolution of the measurement) as range spread *F* in the ionograms measured over Tucumán. This is demonstrated by Figure 4 which presents two consecutive ionograms recorded over Tucumán at 01:40 UT (just before the start of oblique spread structures in Figure 3) and at 01:50 UT (after the start of oblique spread structures in Figure 3) on 25 October. The critical frequency f_oF_2 is relatively high, above 15 MHz. It should be noted that the solar activity was also relatively high on 25 October 2013, solar radio flux $F_{10.7}$ cm was ~160, and that Tucumán is under the equatorial ionization anomaly. The values of f_oF_2 higher than 12 MHz were frequently observed at Tucumán after sunset. The oblique spread structures (spread *F*) were observed under various values of f_oF_2.

3. Propagation of GWs, Analysis, and Results

Propagation velocities and directions are found by slowness search applied for the Doppler shifts that were obtained as single-valued function of time for each sounding path (section 2). The slowness search is often used in seismology and acoustics to find azimuth and elevation of waves detected by a sensor array of *N* elements [*Johnson et al*., 2011; *Chum et al*., 2013]. The minimum number of sensors, *N*, to determine the direction and velocity of propagation is $N = 3$. The signals recorded at different locations ($N = 3$ in our case) are shifted for various values of horizontal slowness components s_x (positive eastward) and s_y (positive northward) to the reference point located at the center of the sensor array and summed (averaged) over the time interval Δt. The slowness is the inverse of apparent horizontal velocity and has the unit of s/m. The aim is to find slowness components s_x and s_y for which the energy of the summed (averaged) signal is maximum in the energy map $W(s_x, s_y)$.

$$W(s_x, s_y) \propto \sum_{t_i=-\Delta t/2}^{\Delta t/2} \left[\sum_{n=1}^{N} \frac{f_{Dn}(t_i + s_x \Delta x_n + s_y \Delta y_n + s_z \Delta z_n)}{N} \right]^2, \quad (1)$$

where f_{Dn} is the Doppler shift measured on the *n*th sounding path at the given time and Δx_n, Δy_n, and Δz_n are the Cartesian coordinates of *n*th sensor (reflection point in our case) relative to the center of the array. We neglect the vertical differences Δz_n ($\Delta z_n = 0$), since all the signals are transmitted at the same frequency of 4.63 MHz (shifted just by ~4 Hz) and hence reflect at about the same height. We selected Δt ~90 min since the configuration of the multipoint CDSS is more convenient for short-period and short-scale to medium-scale

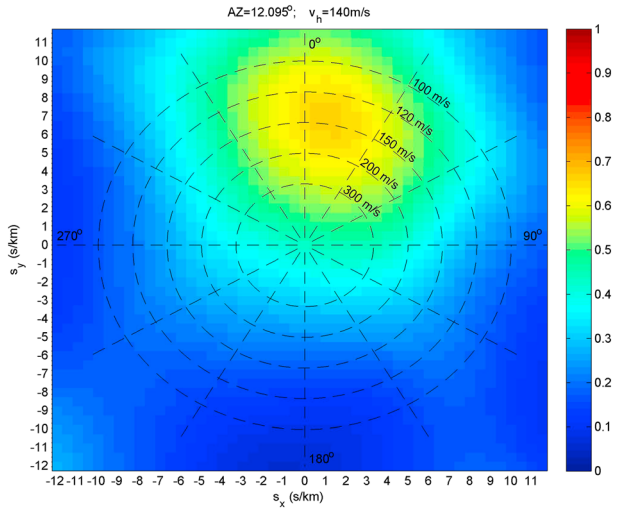

Figure 5. Normalized energy map for various values of slowness components for the interval presented in Figure 1. See section 3 for more details.

GWs. The distances between the individual transmitters are about 100 km, and the distances between the reflection points are around 50 km (Figure 2). These distances allow the determination of time delays and hence the calculation of horizontal velocities with reasonable accuracy only for the short-period and short- (medium-)scale waves. For long-period and large-scale GWs, the uncertainties would be too large. The interval of ~90 min ensures that several "oscillations" of short-period GWs, on which the study is mainly focused, are present in the analyzed time interval. It should be noted that the Doppler sounding is of relatively high time resolution (up to ~10 s) and is, in general, advantageous for investigating the ionsospheric fluctuations of short time scales. To investigate fluctuations with periods longer than ~60 min, it is better to use, e.g., ionosondes that provide more information.

It is convenient to normalize this energy map by the average energy of signals in the specific time window Δt.

$$C(s_x, s_y) = \frac{W(s_x, s_y)}{\frac{1}{N}\sum_{n=1}^{N}\left[\sum_{t_i=-\Delta t/2}^{\Delta t/2} f_{Dn}(t_i)^2\right]}. \quad (2)$$

The elements of the normalized energy map $C(s_x, s_y)$ have similar behavior like coherence (the exact definition of coherence is different). If the signals are identical, then the value of $C(s_x, s_y)$ reaches unity for the slowness components that correspond to propagation velocity and direction of the specific plane wave. Slowness method inherently identifies also multiple coherent waves. However, if one wave dominates over the others, then the maximum in the $C(s_x, s_y)$ map corresponds to this dominant wave. The identification of the dominant wave by the slowness search for multiple-wave occurrence is usually more reliable (robust) than the propagation velocities calculated from time differences obtained by cross-correlation analysis. The slowness search, however, requires more computational time.

To estimate the uncertainties in the velocity and azimuth determined by the slowness search, we repeated the calculation for slightly different time intervals. In addition to the original (0, 90) min interval, we also used the following subintervals: (0, 81) min, (9, 90) min, and (9, 81) min. The values of the best estimates of slowness components s_{xE}, s_{yE} and their uncertainties Δs_x, Δs_y were then determined from these four slightly different overlapping intervals and slowness step (resolution) in the energy map. The formulas used in these calculations are given in Appendix A.

The normalized energy map $C(s_x, s_y)$ for the record presented in Figure 1 is shown in Figure 5. The dominant wave corresponding to the maximum in the $C(s_x, s_y)$ map propagated with the horizontal velocity of 140 ± 6 m/s and azimuth of $12 \pm 3°$. It is necessary to stress that the given uncertainties concern the propagation of the dominant wave and they are not related to the width (span) of the slowness vector which is usually much wider as can be seen in Figure 5. The velocity determined from time differences of the S-shaped signatures [*Chum et al.*, 2010] is 133 ± 31 m/s with azimuth $4 \pm 14°$ for the S-shaped signatures occurring around 21:24 UT, and the velocity estimated from the time differences of steep positive slopes [*Chum et al.*, 2012a] is 139 ± 17 m/s with azimuth $28 \pm 8°$ for the swelling occurring around 22:00 UT. The results obtained by different methods are therefore consistent. We checked this consistency also for other intervals containing the S-shaped signatures in the Doppler shift spectrogram. It is worth reminding that the results obtained by the slowness search represent the average propagation over several periods in the

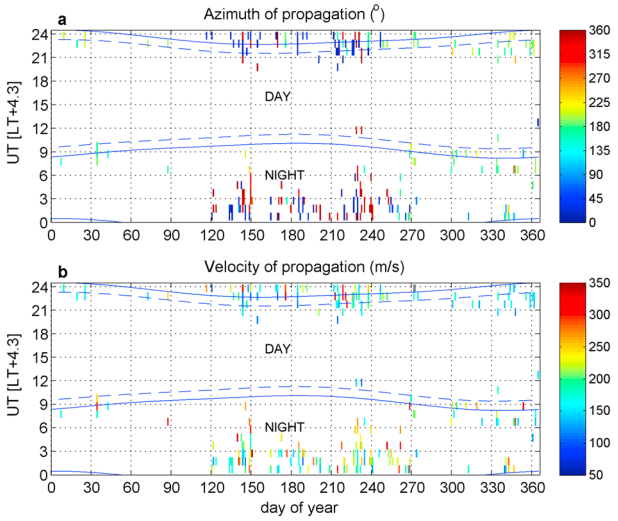

Figure 6. (a) Azimuth and (b) horizontal propagation velocity of GWs as functions of daytime and day of year for GWs in the period range from 4 min to 60 min. Solid (dashed) lines show the times of sunset and sunrise at the altitude of 200 km (0 km).

specific time interval (~90 min), whereas the results obtained from the time differences between S-shaped signatures correspond to propagation of individual disturbances (swellings).

We systematically processed all the data recorded during the first year of measurement from the beginning of December 2012 to the end of November 2013. The analyzed intervals begin at hour (00:00 UT, 01:00 UT, 02:00 UT, …) and have a length of 90 min, so there are 30 min overlaps. We excluded the intervals when approximation by single-valued functions of time was not possible (e.g., intervals containing oblique spread structures), the intervals when a transmitter was not working because of power failure, and the intervals when no signal was received owing to low critical frequency f_oF_2. Figure 6 shows color-coded propagation velocities and azimuths as functions of day of year and daytime (UT = LT + 4.3) for the intervals for which the normalized energy exceeded the value of 0.6 for the dominant wave in at least one subinterval ($\max_i(C(s_x, s_y)) > 0.6$) and the square root of the average signal power, defined by the denominator in equation (2) divided by the number of samples in the interval Δt (Δt ~90 min), exceeded 0.12 Hz ($f_{D\_RMS} > 0.12$ Hz). We also discarded intervals for which the slowness uncertainty for the dominant wave was larger than 2.1 s/km. Figure 6 only displays the velocities lower than 350 m/s, since it is expected that these waves (traveling ionospheric disturbances) can be associated with atmospheric GWs. The ionospheric oscillations caused by geomagnetic pulsations (magnetohydrodynamic waves) or sudden frequency deviation owing to solar X-ray flares may be observed at the same time, within time resolution of measurement, on all sounding paths, and their observed horizontal velocities are close to infinity. Similarly, infrasound waves are observed with high horizontal velocities, if the signals recorded by different transmitter-receiver pairs are correlated. Note also that the uncertainties for velocities larger than ~350 m/s (low slowness values) are relatively large as follows from the distances between reflection points, time resolution of the Doppler shift measurements, and slowness step used for the calculations of $C(s_x, s_y)$ maps. Blue solid and dashed lines in Figure 6 show the time of sunset and sunrise at the altitude of 200 km and on the ground. The results displayed in Figure 6 were computed for the period range 4–60 min; similar results were also obtained in the period subranges of 4–30 min and 30–60 min, the power being usually larger in the former period range. A careful inspection of propagation azimuths shows that roughly meridian propagations dominate. Southward propagation is typically observed in the local summer, whereas northward propagation is more probable in the local winter. Roughly, zonal (mainly eastward) propagation was also observed during the local summer, especially after sunset, in several cases. The majority of 221 intervals displayed in Figure 6 are nighttime observations. The mean (median) value of the observed horizontal velocities is 199 m/s (188 m/s) with standard deviation of the distribution of 60 m/s and 90th and 10th percentiles of 286 m/s and 131 m/s. It should be noted that, in general, the higher the velocity, the higher the uncertainty of measurement. It is interesting to note that if the propagation analysis is based only on the time differences between the S-shaped signatures and/or steep positive slopes [*Chum et al.*, 2012a], then the observed mean velocity is 149 m/s with standard deviation of the distribution 41 m/s (67 such events were analyzed). Since the S-shaped signatures are only observed if the curvature of radius of reflecting surface (horizontal wavelength) is sufficiently small, it is possible to conclude that the GWs with smaller horizontal wavelengths tend to propagate with lower velocities than the GWs with larger horizontal wavelengths. It should also be stressed that the real horizontal velocities cannot be determined without the information about the vertical propagation. The observed horizontal velocities are given by $v_O = v_M/\cos(\theta)$, whereas the real horizontal velocities are given by $v_R = v_M\cos(\theta)$, where v_M is the absolute value of the velocity vector and θ is the angle between the velocity vector and horizontal plane.

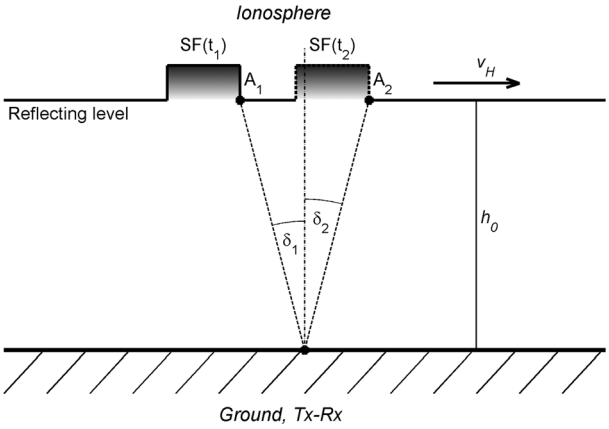

Figure 7. Schematic picture of spread *F* (SF) horizontal movement with velocity v_H. The leading edge is at position A_1 at time t_1 and at position A_2 at time t_2. See section 4 for more details.

We also calculated the neutral wind speeds by the empirical HWM07 (horizontal wind model) at the reflection heights estimated from International Reference Ionosphere (IRI) 2012 model and at the times of measurements displayed in Figure 6. We found that the GWs mostly propagated with observed horizontal velocities approximately perpendicular to or against the neutral winds obtained by the HWM07. Hence, the velocities after subtraction of neutral winds (proxies for intrinsic velocities) are larger than the observed velocities, and their mean (median) value is 234 m/s (230 m/s). This result is consistent with previous measurements [*Crowley and Rodrigues*, 2012; *Chum et al*., 2012a]. It should be noted that the neutral winds can filter specific propagation directions of GWs at any altitude along their trajectory [e.g., *Kelley*, 2009].

4. Propagation of Oblique Spread Structures Related to Spread *F*

Horizontal propagation velocities and directions of oblique spread structures related to spread *F* (section 2) can be estimated from the time differences between the observations of the structures on different sounding paths. It is necessary to stress that it is often difficult to identify the beginnings (ends) of the oblique structures with a sufficient accuracy. We therefore selected only the distinct and clear events for which we estimate that we are able to determine the time differences between the structures on different paths with the uncertainty of ~1 min. Applying this method on the examples of observation presented in Figure 3, we find that the first structure observed from ~01:40 to ~02:30 UT propagated at a velocity of 160 ± 36 m/s with azimuth 102 ± 11°, the second structure recorded from ~03:30 to ~04:10 UT propagated at a velocity of 145 ± 30 m/s with azimuth 96 ± 10°, and the last structure observed from ~05:50 to ~06:30 UT propagated at a velocity of 109 ± 16 m/s with azimuth 86 ± 7°. The time differences were measured manually by clicking at the beginnings of these structures on the Doppler shift spectrogram in MATLAB software. The determination of the positions is therefore partly subjective, and the estimated uncertainty of 1 min is only an average value and for some cases can be better or worse. Fortunately, it is possible to calculate the horizontal velocities (not azimuths) by another independent method which is based on the measurement of the tilt (df_D/dt) of oblique structures in the Doppler shift spectrogram. To understand how the tilt (df_D/dt) is related to propagation velocity, it is useful to look at the situation that is schematically drawn in Figure 7. The location of Tx and Rx is assumed identical for simplicity.

Let us assume that the spread *F* (SF) responsible for the oblique spread structure in the Doppler shift spectrogram propagates from the left to the right in Figure 7. Its leading edge moves from position A_1 at time t_1 to position A_2 at time t_2 with velocity v_H. Let us further assume that small-scale irregularities, much less than the horizontal size of SF region, are present (this assumption will be discussed later). Then, the Doppler shifts $f_D(t_1)$ and $f_D(t_2)$ of backscattered signals are given by relations (3) and (4)

$$f_D(t_1) = 2f_0 \frac{v_H \sin(\delta_1)}{c}, \tag{3}$$

$$f_D(t_2) = -2f_0 \frac{v_H \sin(\delta_2)}{c}, \tag{4}$$

where the meaning of angles δ_1, δ_2 is depicted in Figure 7, f_0 is the sounding frequency (~4.63 MHz), and c is the speed of light. The difference of frequency shifts at times t_1 and t_2 is then given by

$$f_D(t_1) - f_D(t_2) = \Delta f_D = 2f_0 \frac{v_H[\sin(\delta_1) + \sin(\delta_2)]}{c}. \tag{5}$$

The angles δ_1 and δ_2 are, however, also defined by relation (6) as can be understood from Figure 7.

$$\tan(\delta_1) + \tan(\delta_2) = \frac{v_H \Delta T}{h_0}, \quad \Delta T = t_2 - t_1 \,, \tag{6}$$

where h_0 is the height of reflecting level. If the angles δ_1 and δ_2 are small so that $\sin(\delta_1) \approx \tan(\delta_1) \approx \delta_1$ and $\sin(\delta_2) \approx \tan(\delta_2) \approx \delta_2$, then by combining equations (5) and (6), we get the relation (7) for the velocity v_H.

$$v_H = \sqrt{\frac{\Delta f_D}{\Delta T} \frac{h_0 c}{2 f_0}} \,. \tag{7}$$

The velocity v_H is proportional to the square root of the tilt $\Delta f_D/\Delta T$ and to the square root of the reflection height. In other words, for small angles δ_1, δ_2 and constant velocity v_H the tilt $\Delta f_D/\Delta T$ ($\mathrm{d}f_D/\mathrm{d}t$) remains constant. So measuring the tilt in the Doppler shift spectrogram makes it possible to determine the propagation velocity v_H, provided that we know the height of reflection h_0. We therefore limited to the parts of oblique spread structures in Doppler shift spectrogram in which $\mathrm{d}f_D/\mathrm{d}t$ remains constant to calculate the velocity v_H from equation (7). Figure 3 demonstrates that $\mathrm{d}f_D/\mathrm{d}t$ remains constant over significant part of the Doppler shift span for the specific time interval. The measurements of $\Delta f_D/\Delta T$ were done by clicking on the spectrogram in MATLAB software. We estimate that we are able to determine ΔT with the accuracy of ~3 min for most of the observed cases. We note that not all the events are as clear as those displayed in Figure 3. In addition, the tilt can change during some events. That happens mainly for events of longer duration and especially for events that are observed after local midnight (after ~4 UT). Such a change of the tilt is partly seen for the last event in Figure 3. Thus, the accuracy of ~3 min represents an average value. Another uncertainty is from the knowledge of the reflection height. First, the reflection height might not be constant during the spread *F* event; the actual reflection height is of random property, in fact, as can be seen, e.g., in Figure 4b that shows the spread of virtual heights during the spread *F* on 25 October 2013. The width (height span) of spread *F* is, however, much less than its height above the ground. Let us take the value of 25 km as a characteristic half width of the spread *F*. (Note that the true heights should be equal or less than the virtual heights.) Second, as mentioned in section 2, the Tucumán ionosonde was out of regular operation during the considered year; moreover, the installed software provides only virtual heights. We therefore use IRI 2012 model to determine the true reflection heights for $f_0 = 4.63$ MHz and estimate that the height uncertainties from the IRI 2012 model are typically less than 25 km. Summing the estimated uncertainties owing to spread *F* and owing to the use of IRI 2012 model, we get a value of 50 km for the uncertainty in the knowledge of the reflection height h_0. This is approximately one fifth of the typical true reflection height of ~250 km (median value of all the analyzed cases is 255 km). Fortunately, the velocity v_H is proportional to the square root of $\Delta f_D/\Delta T$ and h_0, so the uncertainties in h_0 are still reasonable for rough calculations (estimates) of v_H. Returning to the examples of observation shown in Figure 3, the velocities determined from the tilt measurements are 168 ± 35 m/s for the first event, 150 ± 33 m/s for the second event, and 93±15 m/s for the last event. So the velocities obtained by both methods are consistent. This agreement justifies our assumption of small-scale irregularities used in the mathematical formulation (equations (3)–(7)). The small-scale irregularities associated with spread *F* are usually reported in the literature [*Kelley*, 2009; *Abdu et al*., 2009a, and references therein]. Moreover, the small-scale irregularities cause that a span of Doppler shifts is observed simultaneously, hence fuzzy oblique spread structures in the Doppler shift spectrogram, with contrast to relatively sharp traces in the case of the observations of GWs (S-shaped signatures).

Figure 8 presents the horizontal velocities (values are color coded) estimated from the measured tilt $\Delta f_D/\Delta T$ as functions of day of year and daytime (UT = LT + 4.3) over 1 year from the beginning of December 2012 to the end of November 2013. Altogether, 182 different events were analyzed. The blue solid and dashed lines show the time of sunset and sunrise at the altitude of 200 km and on the ground. It is obvious that oblique spread structures were observed after sunset, during the night, and only in the local summer half of the year, from ~September to ~March (one event was observed in April). They were not observed during the local winter. The occurrence times are thus in relatively good agreement with the scintillation occurrences of GPS signals in Tucumán reported by *Ezquer et al*. [2003].

We also investigated the dependence of propagation velocities and directions on the daytime. Blue error bars in Figures 9a and 9b show the azimuths and horizontal velocities, respectively, obtained from the time differences between oblique spread structures on different sounding paths. Altogether, 64 events were analyzed. The observed (estimated) azimuths range from ~40 to ~130° with the mean value of 84° and standard deviation

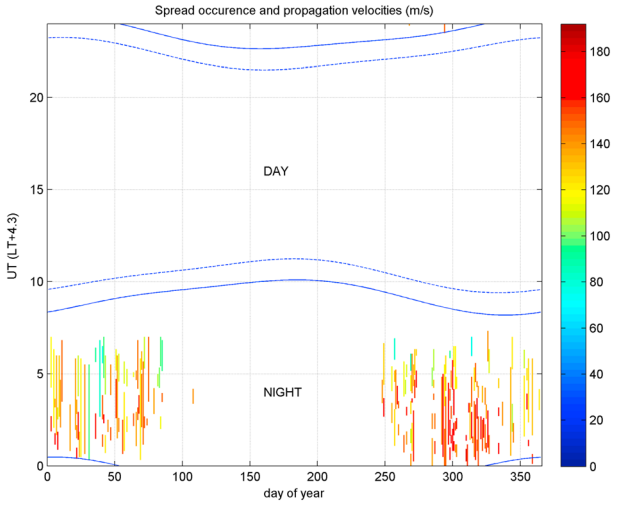

Figure 8. Spread *F* occurrence and horizontal propagation velocities in m/s estimated by the tilt method. See section 4 for more details. Solid (dashed) lines show the times of sunset and sunrise at the altitude of 200 km (0 km).

of the distribution of 18°, and the velocities range from ~79 to ~178 m/s with the mean value of 132 m/s and standard deviation of the distribution of 25 m/s. Magenta error bars show the velocities estimated from the tilt measurement (182 events). These velocities range from ~74 to ~180 m/s with the mean value of 136 m/s and standard deviation 22 m/s. If we apply the tilt method only on the 64 cases for which the time differences were measured, then the mean value is 135 m/s and standard deviation 22 m/s. It is obvious that the velocities obtained by both methods are in a reasonable agreement; the estimated error bars generally overlap. The tilt method gives, in general, a bit larger velocities. The difference of mean values is, however, within statistical uncertainties. A possible explanation for it could be that IRI 2012 model overestimates the reflection heights. The obtained velocities are also in agreement with published values reported from optical observations; e.g., *Terra et al.* [2004] give zonal velocities from 78 m/s to 145 m/s. The eastward propagation was also confirmed by simultaneous optical and GPS measurements [*Haase et al.*, 2011]

There is a tendency for decrease of velocity after ~4 UT in Figure 9. It is necessary to note that for some events we often observed decreasing tilt df_D/dt. This was especially for the events that occurred after ~4 UT. At the same time, the span of Doppler shift was decreasing. This effect is partly seen in Figure 3 for the last event, but there are cases for which this effect is more pronounced. In such cases it was difficult to measure the tilt; we measured the tilt usually at the beginning of the event, so the velocity at the end of the event is expected to be smaller in fact. This effect is also associated with the gradual vanishing of the oblique spread structure in the Doppler shift spectrogram.

According to theory [e.g., *Kelley*, 2009], the nighttime zonal plasma velocities in the *F* region should approach the zonal neutral wind velocities. Hence, the measurements of velocities of the oblique spread structures also provide information about the neutral wind velocities in the *F* region.

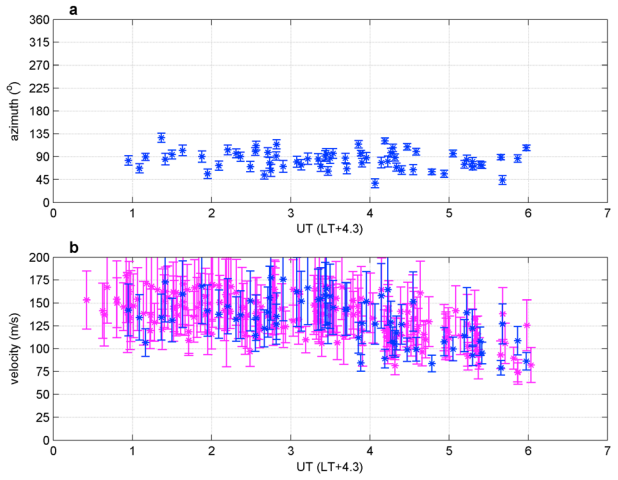

Figure 9. (a) Azimuths and (b) horizontal propagation velocities of oblique spread structures as a function of daytime. Values determined from time differences between different sounding paths are by blue; velocities estimated by the tilt method are by magenta color.

The GWs discussed in section 3 mostly propagate in roughly meridian directions, with contrast to oblique spread structures that propagate roughly eastward. It should be noted that the statistics of GWs mostly cover different days and/or daytimes than the statistics of oblique spread structures. If GWs are observed shortly before the occurrence of oblique spread structure, then these GWs also propagated with significant zonal (eastward) component of velocity. It is, however, necessary to stress that distinct GWs were usually not observed before the oblique spread structures in Doppler shift spectrograms, as demonstrated in Figure 3. It seems from continuous Doppler sounding that the amplitude of GWs is not important for the spread *F* initiation. It is possible that GWs help to destabilize the *F* region, but their amplitude is not critical; so there may be other

mechanisms that are important for the spread *F* initiation. It should be noted in this respect that the model proposed by *Kudeki et al.* [2007] shows that *F* region eastward wind can play a critical role in controlling the structuring of bottomside *F* region and instability growth. However, we cannot exclude that the majority of the observed spread *F* events originated at other places (not over Tucumán), where we do not know the activities of GWs. A detailed analysis of this complicated problem is outside the scope of this experimental paper which is focused on the propagation directions and velocities of GWs and oblique spread structures (spread *F*) and their occurrences. We hope to address the conditions for initiation of oblique spread structures in more detail in the future using multi-instrument observations (continuous Doppler radar, ionosonde, and GPS receiver) and taking into account the state of the ionosphere in the equatorial region.

5. Conclusions

We have presented results of systematic analysis of horizontal propagation of GWs and spread *F* structures at low-latitude ionosphere in the Tucumán region, Argentina. The results are based on measurements by the multipoint continuous Doppler sounding system performed during the first year of the system operation from December 2012 to November 2013. To the best of our knowledge, the continuous Doppler sounding was used for the first time to determine the propagation of spread *F*. The advantage of continuous Doppler sounding compared to optical measurements is the independence from weather conditions.

The oblique spread structures in Doppler shift spectrograms, associated with the spread *F*, were observed at night (after sunset) in the local summer, from ~ September to ~March. They propagated roughly eastward; the mean azimuth calculated from time differences on different sounding paths was 84° with standard deviation of the distribution ~18°. The propagation velocities were calculated by two independent methods: (a) from the time differences between observations of the corresponding structures on different sounding paths and (b) from the tilt (df_D/dt) in the Doppler shift spectrograms. The second method is dependent on the knowledge of reflection heights, which were estimated from IRI 2012 model in our case. Both methods give similar values; a mean value of 132 m/s with standard deviation of distribution of 25 m/s was obtained for method (a), and mean value of 135 m/s with standard deviation of distribution of 22 m/s for method (b). A tendency for the decrease of propagation velocity was often observed after ~ 4 UT (UT = LT + 4.3).

The propagation directions and velocities of GWs were determined by the slowness search. A preference for northward or southward propagation was found; southward propagation was more probable during the local summer. It was found that the GWs propagated mostly perpendicular to or against the neutral winds obtained by the HWM07 at the altitudes of GW observations. Several GW events with roughly zonal propagation were, however, also observed, e.g., roughly eastward propagation was measured after the sunset in the local summer. Most frequently observed horizontal velocities were in the range of ~100–250 m/s.

Appendix A: Formulas for Calculating Slowness (Velocity) Components and Their Uncertainties

The values of the best estimates of slowness components s_{xE}, s_{yE} and their uncertainties Δs_x, Δs_y were determined as follows:

$$s_{xE} = \frac{\sum_{i=1}^{4} \max_i\left(C\left(s_x, s_y\right)\right) \cdot s_{xMi}}{\sum_{i=1}^{4} \max_i\left(C\left(s_x, s_y\right)\right)}, \tag{A1a}$$

$$s_{yE} = \frac{\sum_{i=1}^{4} \max_i\left(C\left(s_x, s_y\right)\right) \cdot s_{yMi}}{\sum_{i=1}^{4} \max_i\left(C\left(s_x, s_y\right)\right)}, \tag{A1b}$$

$$\Delta s_x^2 = \frac{\sum_{i=1}^{4} \max_i\left(C\left(s_x, s_y\right)\right) \cdot \left(s_{xMi} - s_{xE}\right)^2}{\sum_{i=1}^{4} \max_i\left(C\left(s_x, s_y\right)\right)} + ds^2, \tag{A1c}$$

$$\Delta s_y^2 = \frac{\sum_{i=1}^{4} \max_i\left(C(s_x, s_y)\right)\cdot\left(s_{yMi} - s_{yE}\right)^2}{\sum_{i=1}^{4} \max_i\left(C(s_x, s_y)\right)} + ds^2, \tag{A1d}$$

where s_{xMi}, s_{yMi} are the values of slowness components of the dominant wave for the ith subinterval, $\max_i(C(s_x, s_y))$ are the maxima in the normalized (coherence) map $C(s_x, s_y)$ for the ith subinterval, and ds is one half of the slowness step with which are calculated the $W(s_x, s_y)$ and $C(s_x, s_y)$ maps. The last terms in equations (A1c) and (A1d) ensure that nonzero uncertainties are obtained even if we get the same results s_{xMi}, s_{yMi} for all the subintervals. The slowness step of 0.5 s/km was chosen ($ds = 0.25$ s/km) as a compromise between the accuracy and time needed for computation of $C(s_x, s_y)$ maps. Only values that satisfy $\max_i(C(s_x, s_y)) > 0.5$ are considered for the calculations in equations (A1). At least two values $\max_i(C(s_x, s_y)) > 0.5$ with at least one value $\max_i(C(s_x, s_y)) > 0.6$ are required to consider the calculation reliable. Similarly, it was required that $\Delta s_x^2 + \Delta s_y^2 < 2.1$ s/km; otherwise, the measurement was considered unreliable and discarded.

The radial value of slowness s, azimuth AZ, and their uncertainties Δs and ΔAZ are obtained from the following relations:

$$s^2 = s_{xE}^2 + s_{yE}^2, \tag{A2a}$$

$$\phi = \tan^{-1}\left(\frac{s_{yE}}{s_{xE}}\right). \tag{A2b}$$

The $a$tan2 function is used to calculate the four-quadrant inverse tangent in equation (A2b).

$$AZ = 90 - \phi\frac{180}{\pi}. \tag{A2c}$$

If $AZ < 0$, then $AZ = AZ + 360$ to fit into the interval 0–360.

$$\Delta s = \Delta s_x|\cos\phi| + \Delta s_y|\sin\phi|, \tag{A2d}$$

$$\Delta AZ = \tan^{-1}\left(\left(\Delta s_x|\sin\phi| + \Delta s_y|\cos\phi|\right)/s\right)\frac{180}{\pi}. \tag{A2e}$$

The horizontal velocity v and its uncertainty Δv is estimated as

$$v = \frac{1}{2}\left(\frac{1}{s - \Delta s} + \frac{1}{s + \Delta s}\right), \tag{A3a}$$

$$\Delta v = \frac{1}{2}\left(\frac{1}{s - \Delta s} - \frac{1}{s + \Delta s}\right). \tag{A3b}$$

It is important to note that the uncertainties concern the propagation of the dominant wave, not the width of the s vector. This width can be deduced from the slowness maps.

Acknowledgments

The Doppler data are available at http://datacenter.ufa.cas.cz/ under the link to spectrogram archive and/or to 8 h (2 h) spectrograms. The IRI 2012 http://omniweb.gsfc.nasa.gov/vitmo/iri2012_vitmo.html is acknowledged for providing the electron density profile from which the reflection heights were obtained. The NASA National Space Science Data Center http://nssdcftp.gsfc.nasa.gov/models/atmospheric/hwm07/ is acknowledged for providing the source code of the HWM07/DWM07 wind model. The support under grant P209/12/2440 and 13-09778P by the Czech National Foundation is acknowledged.

Alan Rodger thanks Preeti Bhaneja and an anonymous reviewer for their assistance in evaluating this paper.

References

Abdu, M. A., I. S. Batista, B. W. Reinisch, J. R. de Souza, J. H. A. Sobral, T. R. Pedersen, A. F. Medeiros, N. J. Schuch, E. R. de Paula, and K. M. Groves (2009a), Conjugate Point Equatorial Experiment (COPEX) campaign in Brazil: Electrodynamics highlights on spread F development conditions and day-to-day variability, *J. Geophys. Res.*, *114*, A04308, doi:10.1029/2008JA013749.

Abdu, M. A., E. A. Kherani, I. S. Batista, E. R. de Paula, D. C. Fritts, and J. H. A. Sobra (2009b), Gravity wave initiation of equatorial spread F/plasma bubble irregularities based on observational data from the SpreadFEx campaign, *Ann. Geophys.*, *27*, 2607–2622.

Cabrera, M. A., M. Pezzopane, E. Zuccheretti, and R. G. Ezquer (2010), Satellite traces, range spread-F occurrence, and gravity wave propagation at the southern anomaly crest, *Ann. Geophys.*, *28*, 1133–1140, doi:10.5194/angeo-28-1133-2010.

Chum, J., T. Šindelářová, J. Laštovička, F. Hruška, D. Burešová, and J. Baše (2010), Horizontal velocities and propagation directions of gravity waves in the ionosphere over the Czech Republic, *J. Geophys. Res.*, *115*, A11322, doi:10.1029/2010JA015821.

Chum, J., R. Athieno, J. Base, D. Buresova, F. Hruska, J. Lastovicka, L.-A. McKinnell, and T. Sindelarova (2012a), Statistical investigation of horizontal propagation of gravity waves in the ionosphere over Europe and South Africa, *J. Geophys. Res.*, *117*, A03312, doi:10.1029/2011JA017161.

Chum, J., F. Hruska, J. Zednik, and J. Lastovicka (2012b), Ionospheric disturbances (infrasound waves) over the Czech Republic excited by the 2011 Tohoku earthquake, *J. Geophys. Res.*, *117*, A08319, doi:10.1029/2012JA017767.

Chum, J., G. Diendorfer, T. Sindelarova, J. Base, and F. Hruska (2013), Infrasound pulses from lightning and electrostatic field changes: Observation and discussion, *J. Geophys. Res. Atmos.*, *118*, 10,653–10,664, doi:10.1002/jgrd.50805.

Crowley, G., and F. S. Rodrigues (2012), Characteristics of traveling ionospheric disturbances observed by the TIDDBIT sounder, *Radio Sci.*, *47*, RS0L22, doi:10.1029/2011RS004959.

Davies, K., and D. M. Baker (1966), On frequency variations of ionospherically propagated HF radio signals, *Radio Sci.*, *1*, 545–556.

Davies, K., J. Watts, and D. Zacharisen (1962), A study of F2-layer effects as observed with a Doppler technique, *J. Geophys. Res.*, *67*(2), 601–609, doi:10.1029/JZ067i002p00601.

Dou, X., T. Li, Y. Tang, J. Yue, T. Nakamura, X. Xue, B. P. Williams, and C. Y. She (2010), Variability of gravity wave occurrence frequency and propagation direction in the upper mesosphere observed by the OH imager in Northern Colorado, *J. Atmos. Sol. Terr. Phys.*, *72*, 457–462, doi:10.1016/j.jastp.2010.01.002.

Ezquer, R. G., P. M. Kintner, M. A. Cabrera, S. M. Radicella, and B. Forte (2003), Scintillations observed at Tucuman as observed from GPS signals. First results, *Adv. Space Res.*, *31*(3), 741–747.

Fejer, B. G., L. Scherliess, and E. R. de Paula (1999), Effects of the vertical plasma drift velocity on the generation and evolution of equatorial spread F, *J. Geophys. Res.*, *104*, 19,859–19,870, doi:10.1029/1999JA900271.

Fritts, D. C., and M. J. Alexander (2003), Gravity wave dynamics and effects in the middle atmosphere, *Rev. Geophys.*, *41*(1), 1003, doi:10.1029/2001RG000106.

Georges, T. M. (1967), Ionospheric effects of atmospheric waves, *ESSA Tech. Rep. IER 57–ITSA 54*, Inst. for Telecommun. Sci. and Aeron., Boulder, Colo.

Haase, J. S., T. Dautermann, M. J. Taylor, N. Chapagain, E. Calais, and D. Pautet (2011), Propagation of plasma bubbles observed in Brazil from GPS and airglow data, *Adv. Space Res.*, *47*(10), 1758–1776, doi:10.1016/j.asr.2010.09.025.

Hines, C. O. (1960), Internal atmospheric gravity waves at ionospheric heights, *Can. J. Phys.*, *38*, 1441–1481.

Hocke, K., and K. Schlegel (1996), A review of atmospheric gravity waves and travelling ionospheric disturbances: 1982–1995, *Ann. Geophys.*, *14*, 917–940.

Isler, J. R., M. J. Taylor, and D. C. Fritts (1997), Observational evidence of wave ducting and evanescence in the mesosphere, *J. Geophys. Res.*, *102*, 26,301–26,313, doi:10.1029/97JD01783.

Johnson, J. B., R. O. Arechiga, R. J. Thomas, H. E. Edens, J. Anderson, and R. Johnson (2011), Imaging thunder, *Geophys. Res. Lett.*, *38*, L19807, doi:10.1029/2011GL049162.

Kelley, M. C. (2009), *The Earth's Ionosphere, Plasma Physics and Electrodynamics*, 2nd ed., Elsevier, Amsterdam, Netherlands.

Kudeki, E., A. Akgiray, M. Milla, J. L. Chau, and D. L. Hysell (2007), Equatorial spread-F initiation: Post-sunset vortex, thermospheric winds, gravity waves, *J. Atmos. Sol. Terr. Phys.*, *69*, 2416–2427, doi:10.1016/j.jastp.2007.04.012.

Laštovička, J. (2006), Forcing of the ionosphere by waves from below, *J. Atmos. Sol. Terr. Phys.*, *68*, 479–497, doi:10.1016/j.jastp.2005.01.018.

Liu, J. Y., C. S. Chiu, and C. H. Lin (1996), The solar flare radiation responsible for sudden frequency deviation and geomagnetic fluctuation, *J. Geophys. Res.*, *101*(A5), 10,855–10,862, doi:10.1029/95JA03676.

Makela, J. J., and M. C. Kelley (2003), Field-aligned 777.4-nm composite airglow images of equatorial plasma depletions, *Geophys. Res. Lett.*, *30*(8), 1442, doi:10.1029/2003GL017106.

Martinis, C., J. V. Eccles, J. Baumgardner, J. Manzano, and M. Mendillo (2003), Latitude dependence of zonal plasma drifts obtained from dual-site airglow observations, *J. Geophys. Res.*, *108*(A3), 1129, doi:10.1029/2002JA009462.

McNamara, L. F., J. M. Retterer, M. A. Abdu, I. S. Batista, and B. W. Reinisch (2008), F2 Peak parameters, drifts and spread F derived from digisonde ionograms for the COPEX campaign in Brazil, *J. Atmos. Sol. Terr. Phys.*, *70*, 1144–1158.

Nishioka, M., T. Tsugawa, M. Kubota, and M. Ishii (2013), Concentric waves and short-period oscillations observed in the ionosphere after the 2013 Moore EF5 tornado, *Geophys. Res. Lett.*, *40*, 5581–5586, doi:10.1002/2013GL057963.

Otsuka, Y., K. Suzuki, S. Nakagawa, M. Nishioka, K. Shiokawa, and T. Tsugawa (2013), GPS observations of medium-scale traveling ionospheric disturbances over Europe, *Ann. Geophys.*, *31*, 163–172, doi:10.5194/angeo-31-163-2013.

Reinisch, B. W., M. Abdu, I. Batista, G. S. Sales, G. Khmyrov, T. A. Bullett, J. Chau, and V. Rios (2004), Multistation digisonde observations of equatorial spread F in South America, *Ann. Geophys.*, *22*, 3145–3153.

Shiokawa, K., Y. Otsuka, and T. Ogawa (2009), Propagation characteristics of nighttime mesospheric and thermospheric waves observed by optical mesosphere thermosphere imagers at middle and low latitudes, *Earth Planets Space*, *61*, 479–491.

Šindelářová, T., D. Burešová, J. Chum, and F. Hruška (2009), Doppler observations of infrasonic waves of meteorological origin at ionospheric heights, *Adv. Space Res.*, *43*, 1644–1651.

Sutcliffe, P. R., and A. W. V. Poole (1989), Ionospheric Doppler and electron velocities in the presence of ULF waves, *J. Geophys. Res.*, *94*(A10), 13,505–13,514, doi:10.1029/JA094iA10p13505.

Terra, P. M., J. H. A. Sobral, M. A. Abdu, J. R. Souza, and H. Takahashi (2004), Plasma bubble zonal velocity variations with solar activity in the Brazilian region, *Ann. Geophys.*, *22*, 3123–3128.

Vadas, S. L. (2007), Horizontal and vertical propagation and dissipation of gravity waves in the thermosphere from lower atmospheric and thermospheric sources, *J. Geophys. Res.*, *112*, A06305, doi:10.1029/2006JA011845.